On the role of the hierarchical structures in the friction-induced phenomena of directed energy deposited 316L+WC sliding against different counter-bodies

Enrico Saggionetto[a], Tommaso Maurizi Enrici[a], Olivier Dedry[a], Frédéric Boschini[b], Jérôme Tchoufang Tchuindjang[a], Anne Mertens[a]*

a) Metallic Materials Science (MMS)
University of Liège; Quartier Polytech 1
Allée de la Découverte 13 (B52)
4000 Liège, (Belgium)

b) GREEnMat laboratory
University of Liège
Allée de 6 Août, 13 Bât, B6a
4000 Liège, (Belgium)

*Corresponding author. Tel.: +32 4 3669162
E-mail address: j.tchuindjang@uliege.be

Abstract

A tribological study was conducted on a Directed Energy Deposited Metal Matrix Composite made of 316L and tungsten carbides as reinforcements. Pin-on-disc campaign in dry sliding conditions was carried out using counter-bodies with different properties. WC-6Co and Si_3N_4 were selected as main counter-bodies, complemented by Al_2O_3 and stainless steel for a more comprehensive study. The characterization of the wear behaviour considered each tribosystem at all levels, allowing to observe the different friction-induced phenomena at the macro-, micro- and nano-scale. Each counter-body stresses a specific hierarchical structure of the material making it possible to identify two main wear mechanisms: tribo-corrosive vs tribo-chemical.

Keywords (4): Metal matrix composite, Directed energy deposition, Hierarchical structures, Counter-bodies influence.

1. Introduction

The increasing demand of industry for wear-resistant materials is a great challenge that leads to the development of new routes to assess wear properties prior to the real application. Nowadays, different wear-testing machines are available. The pin-on-disc is commonly used in laboratory because of its simple arrangement [1]. With this device, the wear behaviour of materials under dry or lubricated sliding can be investigated. Different parameters can be considered for setting up the test, among which are the applied load, the sliding velocity, the counter-body material and environmental conditions. By varying them separately or together, a wear map of a material can be created [2,3]. However, most of the first wear studies focused on wear mechanisms occurring when two materials of the same class are put in sliding contact, especially metal-metal. The complexity of the wear phenomena increases when two different class of materials are sliding against each other, e.g. ceramic-metals. Moreover, with the development of new materials, more complex wear mechanisms have been observed.

Research on wear-resistant materials has grown in the past years [4,5]. In many metals, the addition of different types of reinforcements enables a wide variety of properties to be achieved [6]. Thus, Metal Matrix Composites (MMC) processed by powder based elaboration routes were seen as a good compromise to improve the wear properties of various metals [6–8]. Furthermore, with Additive Manufacturing (AM) technologies, the development of new MMC has been increased [9]. Among the AM technologies, Direct Energy Deposition (DED) is a suitable technique for the manufacturing of metal coatings, in particular MMC. Many works dealing with the use of DED with various metal-based powder and the addition of tungsten carbide (WC) as reinforcement, have been carried out, leading to the improvement of wear properties [10–15]. Due to ultra-fast cooling rates (10^4-10^5 K/s) during the solidification stage of the DED process and the partial dissolution of WC, out-of-equilibrium phases are formed in the MMC SS 316L+WC [16,17]. In particular, hierarchical macro-, micro- and nano-structures are achieved in as-built samples, as it has been highlighted in a previous work [18]. All of these structures contribute in different way to the wear properties of this MMC under dry sliding conditions, leading to complex wear mechanisms.

When testing wear properties of new MMC with the pin-on disc, the role of the counter-body is often neglected since the attention is mainly focused on the wear behaviour of the complex specimen. This can lead to misinterpretation of the actual wear properties of the MMC under consideration. In fact, the counter-body that is most often selected as the suitable candidate for various alloys under dry sliding conditions is alumina (Al_2O_3), based on both its hardness and its chemical inertia [19–22]. However, fracture toughness and elastic constant have also been taken into consideration as features that can influence wear behaviour [23–29]. As a result, both the brittleness index, which corresponds to the ratio between hardness and fracture toughness and the plasticity index, which is the ratio between hardness and elastic constant, have emerged as more relevant parameters than hardness alone. Accordingly, an increase in both indexes makes the counter-body wear rate higher. Since alumina has low fracture toughness and low elastic constant, both brittleness and plasticity indexes are high thus assuming a possible high wear rate of alumina as counter-body. Debris generated from the wear of the counter-body can actively participate in the wear mechanism of the specimen. Thus, even when aiming simply to assess and understand the wear properties of new materials, considering the counter-body as part of the tribosystem is necessary.

In this work, different counter-bodies were selected to assess the wear properties of the DEDed MMC 316L+WC. Specific attention is given to the mechanical and chemical properties of the counter-bodies and their contribution to the wear behaviour. The classical fundamentals of sliding wear such as delamination, abrasion, adhesion, oxidation are used to interpret the complex wear sequences and mechanisms that occur. This is achieved while combining macro-observations (trend of coefficient of friction, observations of the worn volume for both track and counter-body, morphological features of debris, etc.) with observations of the friction induced layers at a micro-scale as well as various nano-scale characterization approaches such as nano-indentation and XRD. Run-in, cyclical regime and tribolayer concepts that have been highlighted within a previous work [18] are revisited to better explain and unveil the uncommon wear behaviour of the new MMC . Finally, the contribution of the different hierarchical macro-, micro- and nano-structures on the wear mechanism depending on the counter-body is analysed in more depth, in order to bring new insights about the full potential of AM technologies to achieve microstructures with innovative and enhanced properties.

2. Materials and Methods

2.1 Samples fabrication and microstructural characterization

The material used in this work is a Metal Matrix Composite (MMC) coating composed of Stainless Steel (SS) 316L and reinforcements of WC particles (20% in volume). Both powders supplied by Höganäs AB were gas atomized with spherical shape and granulometry between 50 and 200 µm. The MMC coating was deposited on a SS316L substrate using a 5-axis Irepa LC Direct Energy Deposition (DED) system with a Nd-YAG laser source. The laser power was varied between 400-570 W for a corresponding traverse speed of 270-290 mm/min, and the layer thickness was set to 600 µm. SS316L and WC powders were stored in two separate tanks to avoid segregations due to difference in density and carried by an inert gas flow to the nozzle where they were mixed. The stream of mixed powder was then focused into the laser beam by an inert gas flow and directed towards the substrate. The dimensions of the final deposit are 35 x 35 mm side length and 14 mm height. Full details of the manufacturing strategy can be found in our previous works [16,18]. After deposition, 5 mm thick wear samples at 6.3 mm of distance to the substrate were obtained by electro-discharge machining and ground to reach a $R_a < 0.2$ µm.

Fig. 1 shows the microstructure of the MMC. Partially dissolved WC particles are well distributed in an austenitic matrix reinforced by a network of reaction carbides. The so-called reaction carbides result from the partial dissolution of the original WC particles within the matrix and consist of $(W,Cr)_xC_y$ types. In particular, M_4C, M_6C and $M_{23}C_6$ carbides are observed [16]. Moreover, the austenitic matrix is enriched with solute atoms of W (from the dissolution of WC) and Mo (present in ss316L) due to the ultra-fast cooling rates pertaining during the DED process [16]. The resulting hierarchical structure thus combines composite, precipitation and solid solution strengthening mechanisms.

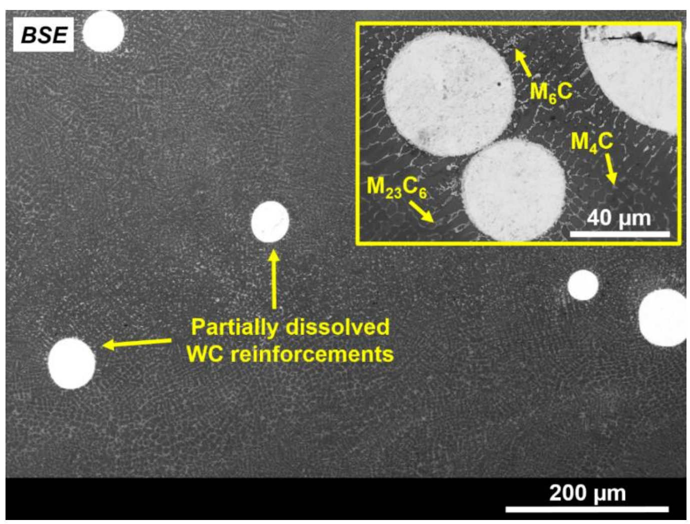

Fig. 1 : Microstructure of the Metal Matrix Composite 316L + 20% (in volume) WC.

2.2 Wear tests

Tribological tests were performed on a CSM high-temperature pin-on-disc tribometer. The wear sample slid against a counter-body pin with a spherical shape of 6 mm diameter. All the tests were performed at room temperature in dry conditions. The sliding speed was 10 cm/s and the applied load was 10 N. Only the counter-body material was changed. WC-6Co and Si_3N_4 were chosen as counter-bodies for the main investigations while Al_2O_3 and AISI 440C martensitic stainless steel (hereinafter referred to as 440C) were used for additional comparison. Table 1 shows the main mechanical properties that influence the wear behaviour and their relationship through the indexes of brittleness and plasticity.

Counter-body	Hardness H [HV]	Fracture Toughness K_{IC} [MPa*m$^{0.5}$]	Elasticity constant E [GPa]	Brittleness Index H/K_{IC}	Plasticity Index H/E
WC-6Co	1400	8-12	610	140	2.29
Si_3N_4	1500	6	320	250	4.69
Al_2O_3	1800	4	380	450	4.74
440C	760	30-80	200	15.2	3.8

Table 1 : Mechanical properties of the counter-bodies, provided by CSM® Instruments.

During the pin-on-disc test, the Coefficient of Friction (CoF) and the Penetration Depth (PDe) were measured by the tangential and the vertical deviation of the pin-on-disc arm sensors, respectively. A reference test was performed three times for both counter-bodies up to the total length of 22000 laps (1520 m at 11mm of sliding radius), and the average was considered for CoF. Then, interrupted tests were performed to better understand specific variations of the CoF. Regarding the interrupted wear tests, the aim was to observe changes at the macro- micro- and nanoscale for both the worn specimen and the counter-body, rather than to calculate the CoF and/or the wear rate. For this reason, only one test for each interrupted test was done with Si3N4 counter-body, while 2 tests were performed with WC-Co as counter-body. Such an approach based on interrupted wear tests that was established in a previous work seemed relevant to better understand the wear behaviour while also highlighting the complex wear mechanisms that can occur [18]. In the same previous work [18], the criteria to distinguish run-in period from subsequent cyclical regimes based on both the evolution of CoF and PDe that were established will still be used in what follows.

2.3 Characterization Methods

Following the wear tests, the worn volume of both specimen and counter-body was estimated by using an Alicona Infinite Focus G5 optical profilometer with the ring-light option. The Wear Rates (WR) were estimated by dividing the worn volume [mm^3] by the sliding distance [m]. The worn track, subsurface and debris were observed through Optical Microscopy (Olympus BX60M) and under a Philips XL30 FEG-ESEM Scanning Electron Microscopy (SEM) using Back-Scattered Electrons (BSE), Secondary Electron (SE) and Energy Dispersive X-ray Spectroscopy (EDS) (10 mm^2 Bruker SDD) detectors. Transversal sections parallel to the sliding direction were obtained by electro-discharge machining to observe the subsurface microstructure of the wear tracks. The subsurface sample was hot mounted using a conductive resin, then ground and polished down to 1 µm prior to chemical etching with aqua regia (15 ml HCl, 5 ml HNO_3, 150ml H_2O). EBSD analysis for phase identification on the transversal section was performed using an accelerating voltage of 20 kV, at a working distance of 15 mm. The resolution was set at 15.5 pixel/µm. Nano-Indention grids (64 x 40 μm^2) were performed on the same area of the EBSD analysis under a HYSITRON TI 950 TriboIndenter using a Berkovich indenter tip mounted on a low load transducer, based on a controlled displacement with the indentation depth set at 100 nm. The load was continuously monitored. A minimum distance of 2 µm was maintained between the successive indents to avoid overlapping of their affected volumes. XRD analyses were performed on debris generated during the reference wear test using a Brucker D8 Discover Twin - Twin model X-ray diffractometer with a Cu Kα radiation source. The scanning range of the 2θ angle was from -10° to 90°, with a step size of 0.02° and a step time of 0.2 s.

3. Results

3.1 Wear tests

3.1.1 Effect of counter-body material on worn volumes

Fig. 2a summarizes the measurements of the worn volume after the reference tests. WC-6Co counter-body wear rate is almost negligible, while that of Si_3N_4 is ten times higher. In contrast, the wear rate of the composite against WC-6Co as counter-body is more than three times that using Si_3N_4. In addition, while the average widths of both worn tracks are similar, there is a significant difference within their average depth. The depth achieved using WC-6Co as counter-body is more than five times higher than the one using Si_3N_4. The scattering on the depth of the worn track (Fig. 2b) reveals higher values for the track generated against WC-6Co compared to that of Si_3N_4. Therefore, both the shape and the smoothness of the final worn volume is influenced by the nature of the counter-body material.

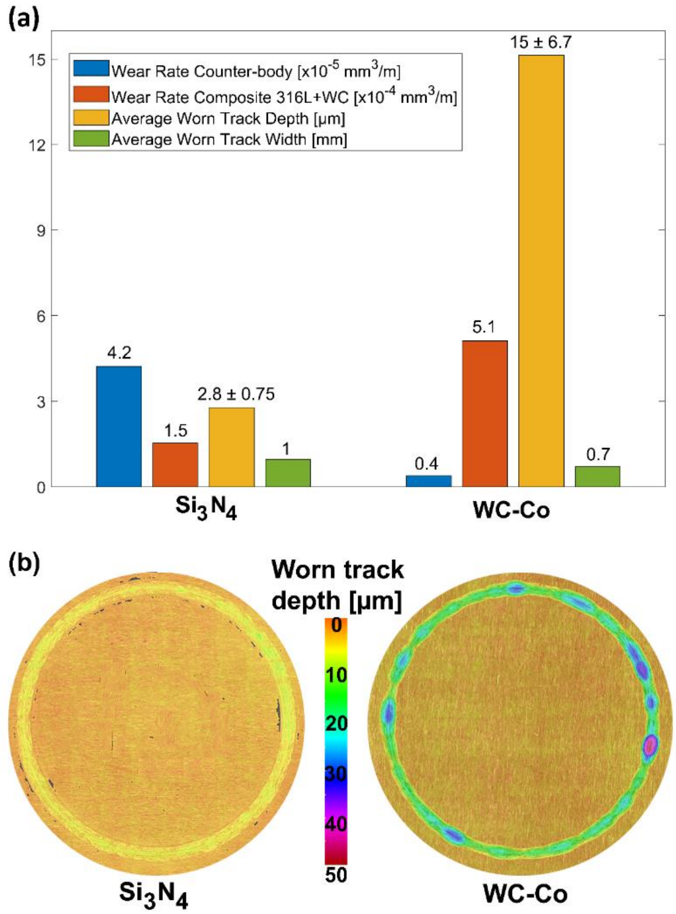

Fig. 2 : Measurements of counter-bodies and composite worn volumes after the reference test (a) and scattering on the worn track depth (b).

3.1.2 CoF and PDe evolution

Typical evolution of the CoF and PDe recorded during the tests using Si_3N_4 and WC-6Co as counter-bodies are shown in Fig. 3. An initial run-in period [18,30] followed by a cyclical regime was observed in both the reference tests. The average CoF is 0.87 and 0.6 using Si_3N_4 and WC-6Co as counter-body respectively. Therefore, the average CoF using Si_3N_4 is very high and close to 1. In addition, such a CoF represents an increase of almost 45% compared with the average value obtained when using WC-6Co as counter-body.

The trend of the CoF with both counter-bodies is similar during the first 1000 laps. In this period, a first rise of the CoF until 0.6 is followed by a decrease until 0.5. With Si_3N_4 the CoF then exhibits a second rise followed by a first sharp drop that corresponds to the beginning of the cyclical regime (laps = 1300). The trend of the CoF during a cyclical segment is characterized by an initial sharp drop, followed by a sharp rise until it stabilizes at a high value (0.87). This trend is repeated cyclically during all the reference test (orange rectangles in Fig. 3a). The PDe, which considers both specimen and counter-body height variations, exhibits an almost steady state during the run-in period and then it increases for all the duration of the test until 0.35 mm, showing some oscillations.

The run-in period length is almost four times higher when WC-6Co is used as counter-body compared to Si_3N_4 (green rectangles in Fig. 3). After the first 1000 laps where the evolution of the CoF is similar to the one observed with Si_3N_4, the CoF with WC-6Co exhibits a first smooth increase until a value of 0.7 at 8000 laps. Then, a cyclical segment starts with a drop of the CoF (orange rectangles in Fig. 3b), followed by a second smooth increase until the CoF rises abruptly and stabilizes again (laps = 13000). The PDe shows a low increase within the run-in period before stabilizing upon entering the cyclical regime. The same trend corresponding to a low increase up to a steady state value for the PDe occurs again within the subsequent cyclical segment, reaching a final value of 0.13 mm at the end of the reference test, which is almost three times less than the PDe of the test using Si_3N_4 as counter-body. Only a small decrease of the PDe is observed between 14000 and 16000 laps, which corresponds to the stabilization of the CoF.

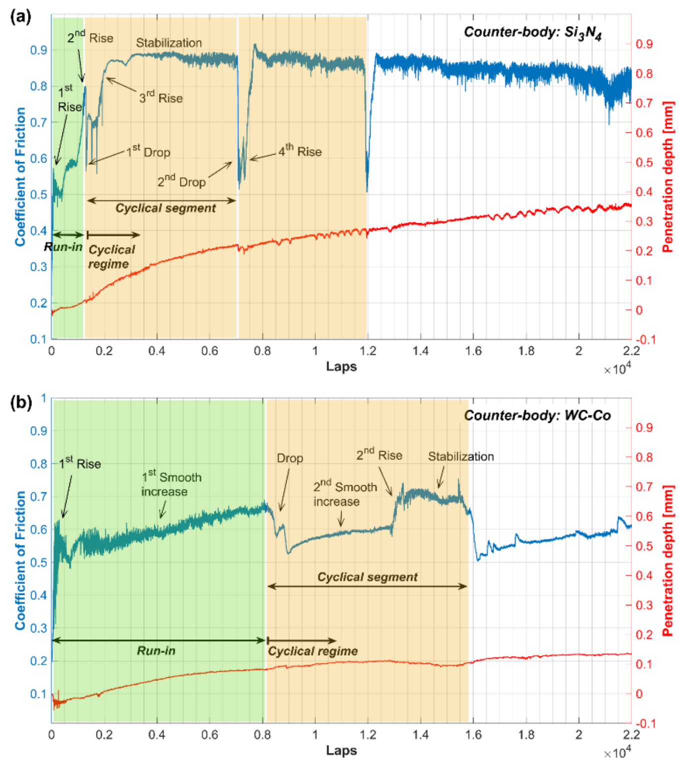

Fig. 3 : Evolution of the Coefficient of Friction (CoF) and Penetration Depth (PDe) of the composite sliding against Si_3N_4 (a) and WC-6Co (b) recorded during pin-on-disc tests.

3.2 Macroscopic changes within both the worn track and the counter-body

3.2.1 316L + WC against Si_3N_4

During the first laps of the run-in period (Fig. 3a), the central part of the track is the first area to be worn (Fig. 4a). The slight grooves visible in Fig. 4b are the result of material pullout that generates debris, which then behave like hard particles [31]. Debris is made of a mixture of material originating from both counter-body and the cladded composite. As the virgin metal is exposed to the environment, oxidation of the debris occurs [32], which is also highlighted by EDS analysis (Fig. 4b.) The compaction of debris in small islands around or over the fractured WC reinforcements also occurs subsequently [33].

The drop in CoF at the beginning of the cyclical regime (Fig. 3a) corresponds to the presence of a layer of oxides, which is debris generated from the counter-body Si_3N_4. As matter of evidence, numerous irregular dark spots (Fig. 4c) enriched with both Si and N are found on the wear track

(Fig. 4d). Despite the presence of some grooves occurring during the run-in period, there are still some areas corresponding to the original surface of the unworn composite (Fig. 4d).

The layer of oxides is compacted as the wear test progresses, leading to the stabilization of the CoF at high values (Fig. 3a). The compaction follows the sliding direction (Fig. 4e-f). EDS analysis (Fig. 4f) carried out on the compacted oxide layer reveals a high concentration of elements from both counter-body and composite. Some areas on the compacted oxide film are delaminated and torn (Fig. 4e). As consequence, sharp debris is generated (Fig. 4e). The delamination reveals the presence of holes underneath, which may subsequently entrap further debris (Fig. 4f).

A general view of the worn track and counter-body after the reference test is shown in Fig. 4g-h. The surface of the worn track shows smooth features with shallow grooves following the sliding direction and some delaminated areas. The Si_3N_4 counter-body reveals a circular, flat and smooth worn surface with a radius of 1.4 mm, and few attached debris.

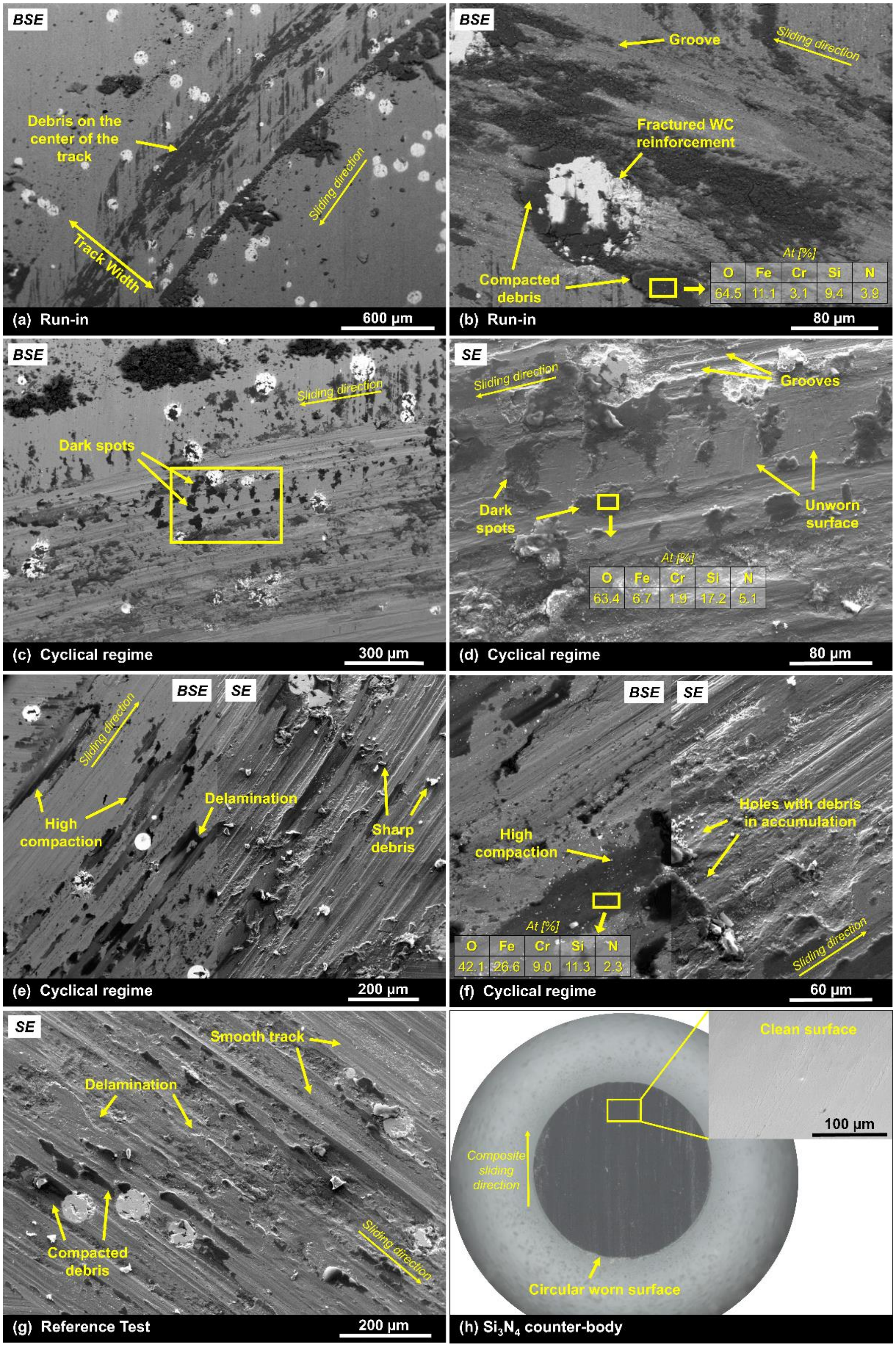

Fig. 4 : Evolution of the worn surface of the composite sliding against Si_3N_4, referring to changes in the CoF (Fig. 3a). Debris spread on the track and first grooves during the run-in (a, b). Transfer of material from the counter-body to the composite during the cyclical regime (c, d), followed by high compaction and delamination of the oxide layer (e, f). Smooth wear of the track (g) and worn counter-body (h) after the reference test.

3.2.2 316L + WC against WC-6Co

With WC-6Co as counter-body, during the first laps of the run-in period (Fig. 3b), plastic flow [34,35] and delamination [8,12–14,36,37] will generate debris (Fig. 5a). As for the run-in period of the test with Si_3N_4 (section 3.2.1), debris will undergo oxidation, as revealed by the EDS profile composition (Fig. 5b).

Oxides are spread along the track during the run-in, with a preferential accumulation in front of the WC reinforcements that act as barriers. Thus, many U-shape islands are formed (Fig. 5c), leading to the drop in CoF that occurs at the beginning of the cyclical regime (Fig. 3b). The so-called U-shape islands give rise to "shadow areas" that correspond to debris free-zone behind the WC reinforcements [10] (Fig. 5d).

The debris accumulated in the U-shape islands are compacted as the wear test proceeds, especially during the smooth increase of the CoF within the cyclical segment (Fig. 3b). Once compaction is achieved, spalling is assumed to occur together with cracks within the debris prior to the subsequent tearing off the loose parts [38] . Such a phenomenon leads to the disappearance of the U shape (Fig. 5e) and the rise in CoF (2^{nd} Rise in Fig. 3b). The debris compacted after being stalled is widespread over the surface, its size ranging between 20 and 30 µm. The massive debris is then crushed into smaller debris (~1 µm) which form the U-shape islands (Fig. 5f) during the "stabilization" segment of the CoF (Fig. 3b). The U-shape islands reformation sets the end of a cyclical segment.

A general view of the worn surface and counter-body after the reference test is shown in Fig. 5g-h. The surface of the composite is severely worn, with holes in front of the WC reinforcements and deep grooves following the sliding direction. Areas behind WC reinforcements are protected from any wear phenomena, thanks to the barrier properties provided by the WC reinforcements.

The WC-6Co counter-body exhibits an oval worn surface of 1.2 mm and 1 mm perpendicularly and parallel to the sliding direction respectively (Fig. 5h). A dark discontinuous layer of debris covering the original bright WC-6Co cermet is present on the worn surface (Fig. 5h).

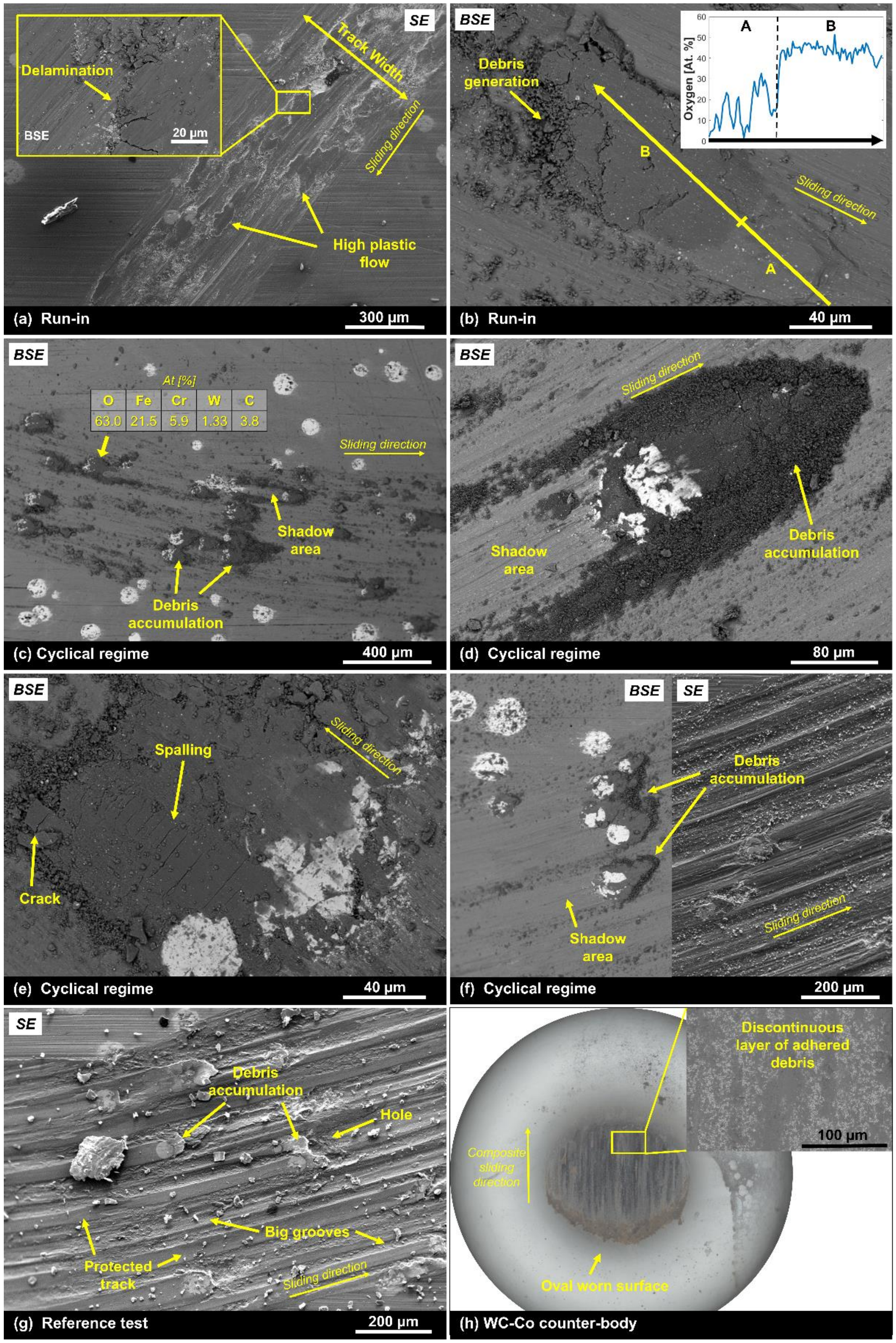

Fig. 5 : Evolution of the worn surface of the composite sliding against WC-6Co, referring to changes in the CoF (Fig. 3b). High signs of plastic flow phenomena during the run-in (a, b). Formation (c, d), compaction (e) and reformation (f) of the U-shape islands. High wear of the track (g) and worn counter-body (h) after the reference test.

3.3 Effect of friction-induced phenomena on the subsurface

During the wear test, the microstructure beneath the surface is affected by friction-induced phenomena, as a Mechanically Mixed Layer (MML) and a Plastic Deformed Layer (PDL) are formed.

3.3.1 Microstructural features of the friction-induced layers

Fig. 6 illustrates the MML formed against the two counter-bodies during the reference tests. The MML formed against Si_3N_4 looks more regular and homogenous (Fig. 6a) than that formed against WC-6Co (Fig. 6b). In addition, the MML formed with Si_3N_4 (5-6 μm) looks thicker than the one achieved with WC-6Co (1-2 μm). The formation of the MML is caused by very large plastic shear strains produced at the sliding interface between counter-body and composite and by the large strain gradients in the near surface material during sliding [39]. As a consequence, the original reaction carbides and the WC reinforcements are fractured and mixed within the matrix (Fig. 6c-d). It has long been established that plastic deformation, material transfer and mechanical mixing involving either the specimen, the counter-body and the debris occur as sliding goes on [40]. Therefore, the oxides formed on the surface that become more compact undergo cracks and subsequent delamination prior to their incorporation into the MML below. This mechanism is observed in large areas for the composite sliding against Si_3N_4 (Fig. 6c-e), while it is localized only within very few holes left by partial fracture of the WC reinforcements for the composite sliding against WC-6Co (Fig. 6f).

The depth of the PDL is similar for both counter-bodies, which is around 8-10 μm. Reaction carbides present within the PDL are influenced by the shear strains generated during the sliding, as they are visibly deformed following the sliding direction (Fig. 6a-b).

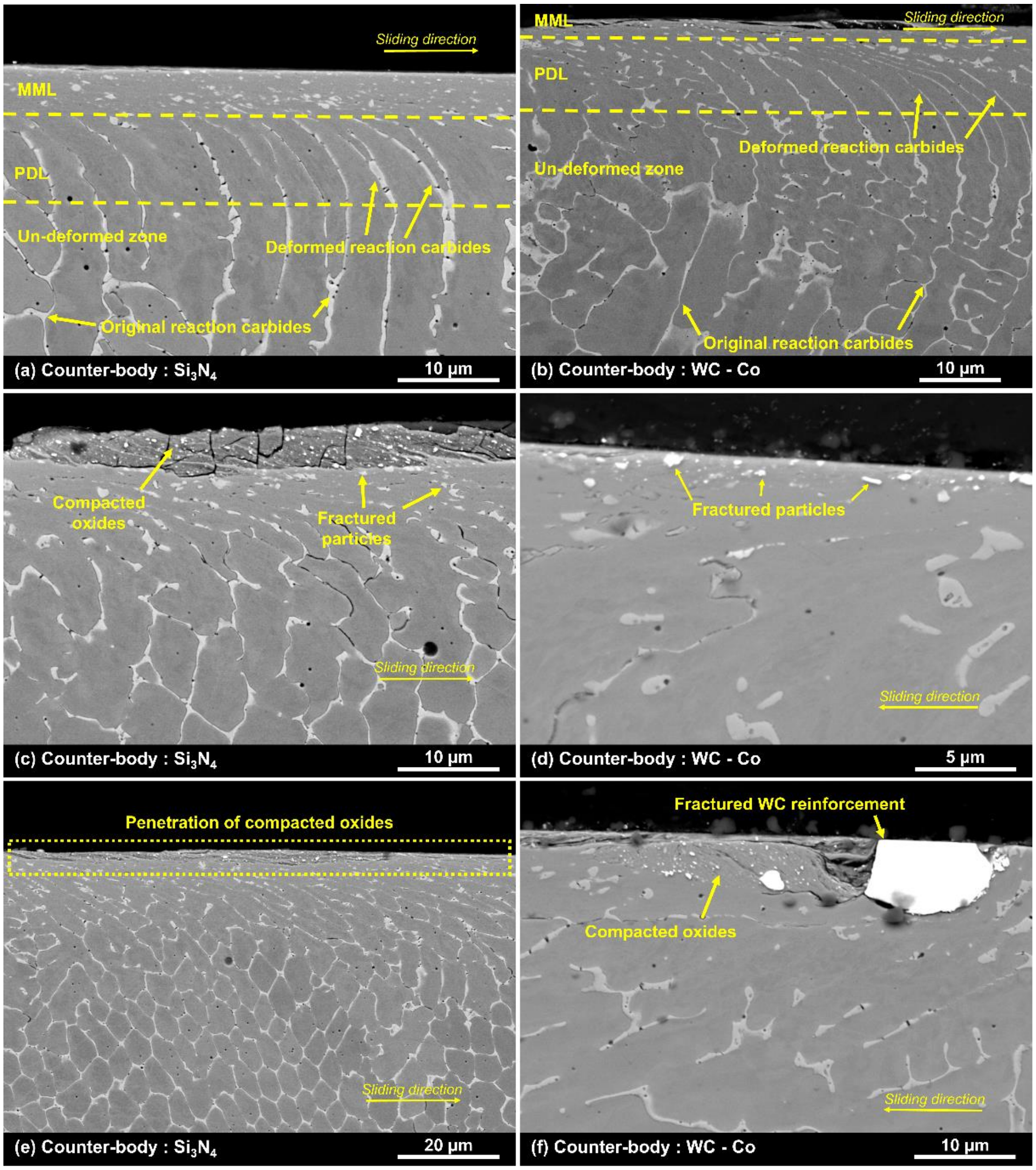

Fig. 6 : Friction-induced layers generated with Si_3N_4 (left) and WC-6Co (right). Depth of the friction-induced layers (a, b), features of the MML (c, d) and penetration of compacted oxides into the subsurface (e, f).

3.3.2 Phases identification through EBSD analysis

Fig. 7a-b shows the phase map after EBSD analysis. The main phases and crystal lattices used for indexing both EBSD maps are listed in the legend. Close to the surface, many spots representing either the iron-rich ε phase or the iron-rich α' phase, which correspond to HCP and BCC crystal lattices respectively, are indexed. Far from the surface, iron-rich γ phase with FCC crystal lattice is found within the matrix. More details on the indexed phases within the reaction carbides can be found in our previous work [16]. The patterns quality of both EBSD analyses (Fig. 7c-d) reveal the existence of a hardly indexed layer which looks dark and where both ε and α' phases are indexed. The low quality of the indexation may be due to the distortion within the heavily deformed metal lattice structure [21] and/or the presence of nanostructures that are difficult to detect using EBSD analysis [41]. These features are typical of friction-induced phenomena, which also affect the hardness of the subsurface microstructure. The depth of this heavily deformed layer corresponds to the combined thickness of both MML and PDL zones [21] (section 3.3.1). Deeper insights are given in the next section.

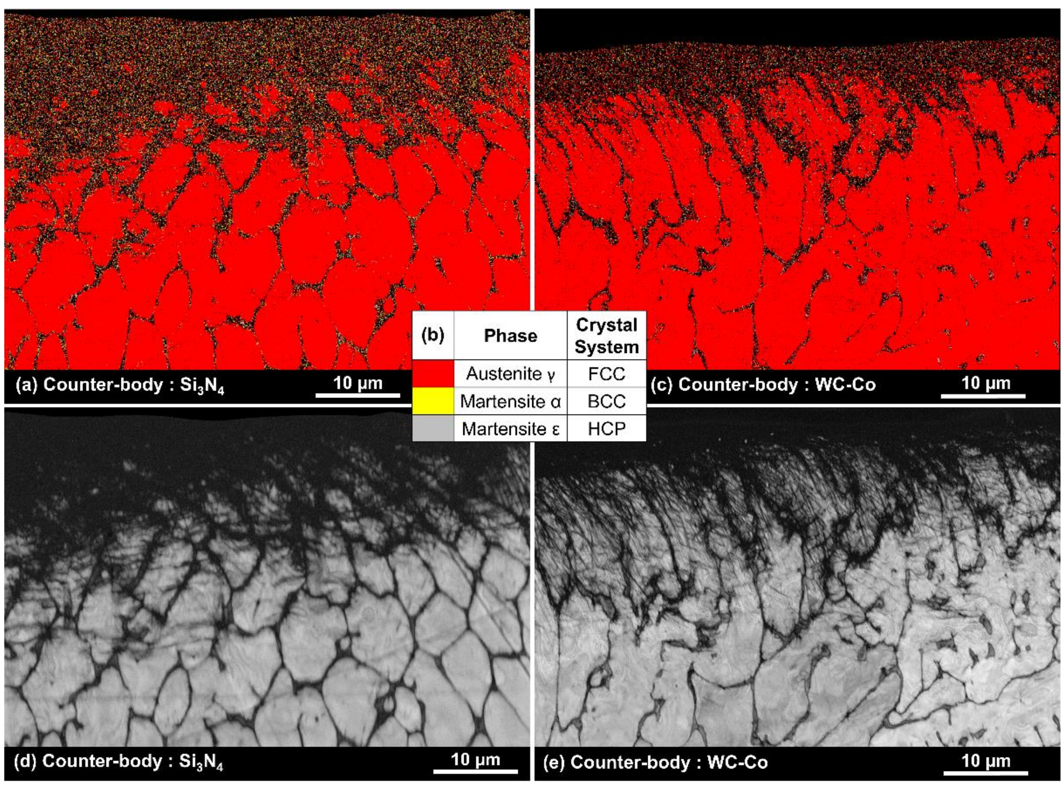

Fig. 7 : Phase maps (a, c), phase list (b) and pattern quality (d, e) of the EBSD analysis on the subsurface microstructure after the reference tests (reaction carbides are not shown for more clarity).

3.3.3 Impact of friction-induced phenomena on nano-hardness

Fig. 8a-b shows a typical nano-hardness map of the subsurface microstructure after the two reference tests. Based on colour change and as also shown by [22,36,42], the nano-hardness decrease from top to bottom. Furthermore, three zones can be identified in the subsurface using both counter-bodies, whose depths correspond to those of the modified layers as highlighted by microscope observations (section 3.3.1). These three zones are as follow: the top MML, the underlying PDL and the more internal un-deformed zone. The MML has the highest hardness, with a different average value between the tribo-system with Si_3N_4 where it reaches a maximum of 8.5 GPa, while the tribo-system with WC-6Co as counter-body has an average hardness of 7.8 GPa. On the other hand, the PDL of both subsurfaces has similar average nano-hardness, which is around 6 GPa. Finally, in the un-deformed zone, the average nano-hardness of the matrix is around 4 GPa. Some areas reveal a nano-hardness higher than 10 GPa, corresponding to reaction carbides present in the microstructure [43].

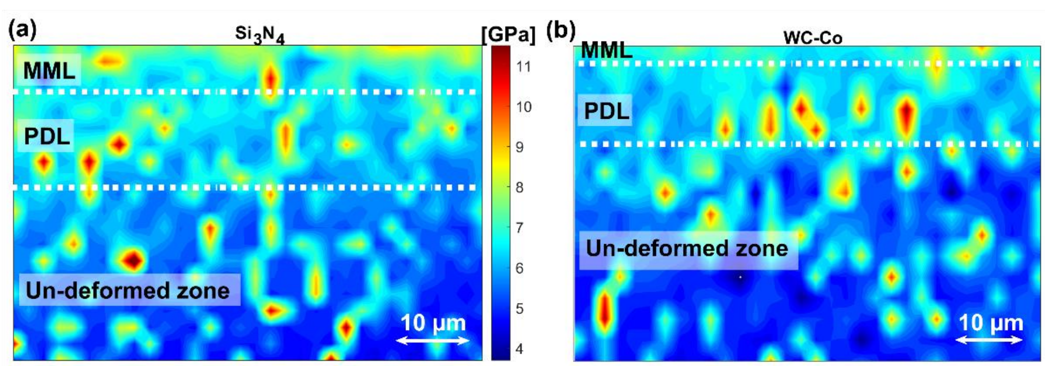

Fig. 8 : Nano-hardness maps of the subsurface within as-polished cross sections after the dry sliding reference tests on 316L+WC MMC against Si_3N_4 (a) and WC-6Co (b).

3.4 Morphological and compositional features of debris

Debris collected after the reference wear tests is mostly green with few orange areas for the test using Si_3N_4 (Fig. 9a) and orange and black for the one with WC-6Co (Fig. 9b). Bright metallic platelets up to a size of 100 µm are found after both reference tests. They originate from the delamination of the composite in the initial stage of the wear test, whereas all powder-like wear debris (~1 µm of size) is generated by oxidative phenomena [44] (Fig. 9). Compacted debris with sharp edges is found only for the test ran while using Si_3N_4, whereas a U-shape island of compacted oxides is present when considering WC-6Co as counter-body. The wear debris generated during the run-in period of the tests exhibit a black contrast for both counter-bodies. Indeed, the transition between the run-in period and the cyclical regime is also associated with a change in the appearance of the debris [45].

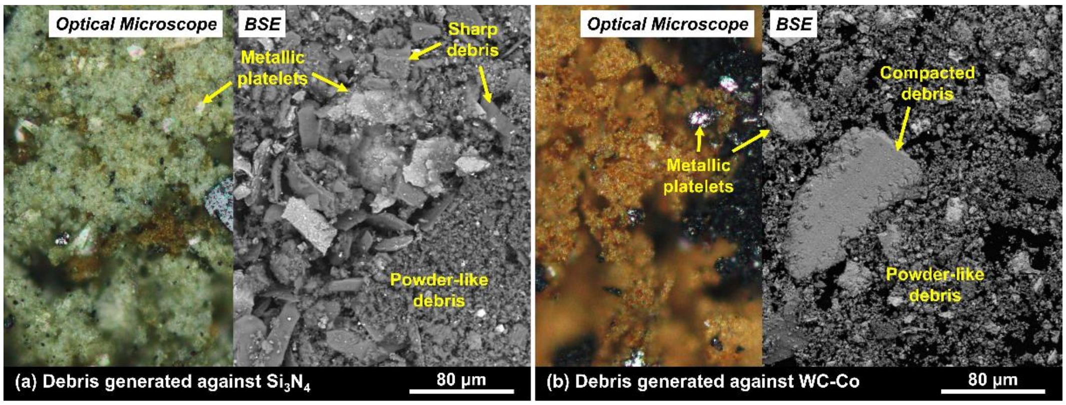

Fig. 9 : Overview of the debris generated during the reference tests. Using Si_3N_4 as counter-body, mostly green with few orange areas and sharp debris is generated (a). Orange and black debris and big compacted islands of debris is generated using WC-6Co (b).

XRD patterns of debris collected after the two reference tests (Fig. 10) reveals the presence of many shallow peaks. The main phases within the debris and their related diffraction patterns are shown in Fig. 10. The dominant phase within debris originated from both tribosystems is austenite (Fe γ), which is identified at $2\theta = 43°$ in both patterns. The diffraction pattern of Fe α exhibits two main peaks at $2\theta = 43°$ and 45°, the first one being superimposed with the austenite peak [46]. Thus, martensite is identified in the debris from the test with WC-6Co, as the width of the peak at $2\theta = 43°$ is higher in the XRD pattern of debris generated using WC-6Co than in that with Si_3N_4. The diffraction pattern of Cr_2O_3 matches both debris patterns only for the peak at $2\theta = 36°$. However, its position is slightly shifted. A similar scenario is observed for the FeO(OH) phase at $2\theta = 36°$ and 40°. WC is well identified in both patterns at $2\theta = 36°$ and 48°, as also shown by [47]. Finally, the Si_3N_4 phase was present within debris of the test with Si_3N_4, showing a match at $2\theta = 35°$ and 70°, as also shown by [48]. The intensity of the peaks is affected by the crystallinity of the phases. Indeed, it has been well established that Solid State Amorphization (SSA) can occur during the wear test, thus introducing chemical and/or structural disorder by various mechanical deformation, which leads to an amorphous structure [41,49].

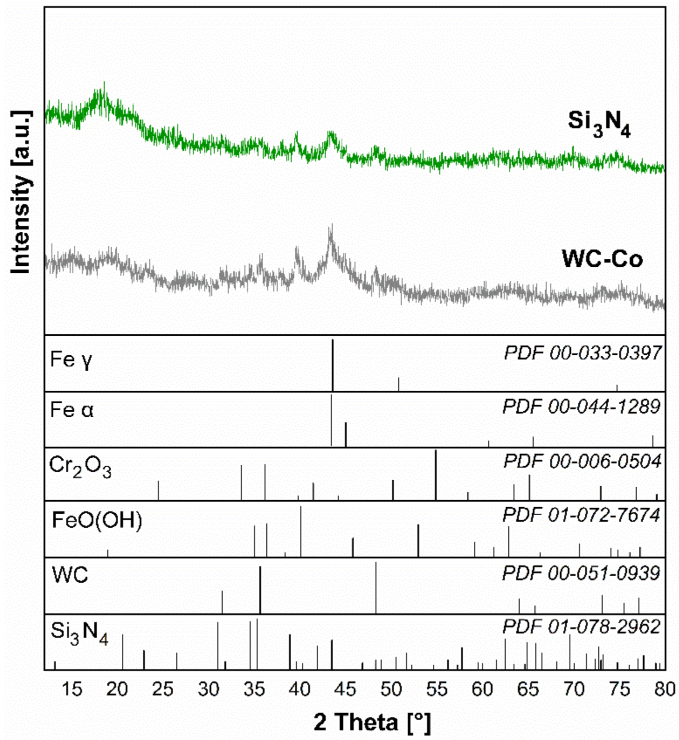

Fig. 10 : XRD patterns of debris generated against Si_3N_4 and WC-6Co during the reference test.

4. Discussion

4.1 Enhancements of wear mechanisms

CoF and PDe can be determined directly during wear tests. Their evolution makes it possible to characterize the wear regime, especially while specifying whether it is cyclical or not. However, this distinction may sometimes require long lasting tests to establish the frequency for the variations of such coefficients. In addition, CoF and PDe remain macroscopic parameters, which do not provide direct qualitative and quantitative information about wear. For instance, wear rates are provided through additional analysis including the assessment of the worn volume. Furthermore, wear mechanisms that are important for understanding the influence of microstructural parameters on the wear phenomenon, cannot be determined based on CoF and

PDe. In what follows, the tribolayer concept will be reviewed with the purpose of adapting its features to specific tribosystems that are studied in this work. Then, defined wear mechanisms as observed within both tribo-systems will be discussed.

4.1.1 The nature of the tribolayer

The tribolayer is defined as a protective layer of oxides that prevent both counter-body and specimen from further wear. Its formation occurs during the run-in period, until it reaches a certain thickness and stability [50–52]. The stabilization corresponds to the decrease of the friction between the materials pair, indicated as the first drop within CoF evolution with both counter-bodies (Fig. 3). In addition, such a decrease of the CoF may be associated to the beginning of the cyclical regime and to the end of the run-in period. Therefore, in this work, the run-in is defined as the period necessary for the appearance of a stable tribolayer that reduce the friction. During the beginning of the run-in, the friction between the materials pair increases, as shown by the first step increase in CoF until a value of 0.6 is reached with both counter-bodies (indicated as '1st Rise' in Fig. 3a-b). At this stage, the contact between the hard counter-body and the softer MMC leads to the generation of metallic platelets from the specimen (Fig. 9), in agreement with the delamination theory of wear [53]. Metal wear debris rich in Fe and Cr (Fig. 4b and Fig. 5b) is comminuted with the progress of the wear test. As consequence, debris particles are heavily deformed, releasing large amounts of heat that enhance their oxidation [50]. Moreover, it is well established that the friction between two materials can increase the local temperature [54], thus also promoting the oxidation of the debris. After this first delamination period that is similar for both counter-bodies, the phenomena that will trigger the appearance of a stable tribolayer and the end of the run-in will be different depending on the counter-body.

With WC-6Co, the subsequent first smooth increase of the CoF up to 8000 laps (Fig. 3b) is related to the formation of the tribolayer. Indeed, oxides are spread along the track, accumulating preferentially in front of the WC reinforcements forming the U-shape islands (Fig. 5c-d). Therefore, with WC-6Co, the WC reinforcements will trigger in the formation of the tribolayer, as numerous U-shape islands made of oxides will be formed. When the U-shape islands reach a certain thickness, the tribolayer becomes stable, preventing the direct contact between counter-body and specimen and thus, decreasing the friction (indicated as 'Drop' in Fig. 3b). It is the ability of oxides to compact that affects the stabilization of the tribolayer. In particular, the little size (~1 µm) of all the powder-like wear debris (oxides) (Fig. 9) allows to achieve good compaction [55], enhancing the stabilization of the tribolayer.

On the contrary, the tribolayer formed with Si_3N_4 as counter-body has a different nature. During the first delamination period where debris from the specimen are generated, the counter-body that is also worn will release debris due to the contact with the hard WC reinforcements (Fig. 4b). The high amount of debris on the track surface from specimen and counter-body (Fig. 4a) lead to the first sharp increase of the CoF up to 0.8 at 1300 laps (Fig. 3b). Subsequently, adhesive wear occurs between the counter-body Si_3N_4 and the specimen. In particular, Si-rich debris from the counter-body adheres over the surface of the specimen and become oxidized, participating in the formation of the tribolayer (Fig. 4c-d). It is because of the significant amount of many dark spots corresponding to Si-rich oxides present over the surface that the tribolayer will become stable enough to decrease the friction between specimen and counter-body (indicated as '1st Drop' in Fig. 3a).

4.1.2 Tribo-corrosive wear with WC-6Co

As explained in the previous section, with WC-6Co as counter-body the tribolayer is characterized by many U-shape islands made of oxides (Fig. 5c-d). After its stabilization and the decrease of the CoF, the U-shape islands start to over-compact and undergo fracture, leading to spalling and cracks (Fig. 5e). The CoF will increase smoothly (Fig. 3b) as the compaction proceeds, while oxides U-shape islands will start vanishing. Furthermore, a severe pull-out may also occur within the U-shape oxides island, as observed within the debris collected after the reference wear test (Fig. 9b). Therefore, a hole will be formed ahead of the WC reinforcements (Fig. 5g). With these conditions, the direct contact between counter-body and specimen occurs, leading to a steep increase of the CoF (indicated as '2^{nd} Rise' in Fig. 3b). The same phenomena that characterized the run-in period occur again. In particular, the subsequent CoF stabilization (Fig. 3b) will be associated with the reformation of a new tribolayer (Fig. 5f), that will also set the beginning of a new cyclical segment from which a wear sequence similar to the one previously described will start again.

The cyclical formation and break-down of the tribolayer strongly influence the friction-induced layers that are formed within the subsurface [13]. During the run-in period, the MML starts to form due to the high stresses generated by the contact between counter-body and specimen. This leads to the fracture of both the WC reinforcements and reaction carbides, whose particles are mixed with the matrix (Fig. 6d). As a consequence, the MML is similar to a hard metal matrix composite with a hardness higher than the virgin microstructure, as revealed by the nano hardness map (Fig. 8b) [56]. That is the reason why the MML will undergo delamination when it comes into direct contact with the tough and stiff WC-6Co counter-body, leading to a thin appearance with a non-homogeneous distribution (Fig. 6b). As a consequence, the PDL underneath the MML is exposed. The PDL is characterized by the presence of deformed reaction carbides together with α' (BCC) and ε (HCP) martensite within the matrix, as revealed by EBSD analysis (Fig. 7b). Since the virgin matrix is fully austenitic, a phenomenon known as friction-induced martensitic transformation will occur during the wear test [36,57]. The parent austenite is reported to undergo different martensitic transformations, the first one that is ascribed to a direct mode leading to α' martensite and the second one occurring via an intermediate transformation through the ε martensite [58,59]. Both martensites can also coexist. The tendency to form each type of martensite will be influenced by the chemical composition, the temperature and also the stress within the alloy, all these features affecting the relative free energy of γ, ε and α' as well as the Stacking Fault Energy (SFE) of γ phase [59]. It has been established that higher SFE decrease the wear resistance of materials [60]. Therefore, Cr, Mo and W that are known as alloying elements that strongly decrease the SFE should increase the wear resistance [61]. Since these elements are mainly present in the reaction carbides of the composite while being less present in the neighbouring matrix [16], the latter should exhibit a high SFE making it prone to the friction induced martensitic transformation.

Martensite can affect both the oxidation and the corrosion resistance [36,62]. Therefore, since the PDL is exposed to the counter-body, martensite will be subjected to atmospheric corrosion through tribo-corrosive wear mechanisms. In particular, the corrosive product FeO(OH) is formed, as revealed by the typical orange coloration of this phase as shown within Fig. 9b and by XRD analysis (Fig. 10) [63]. These phenomena occur mostly in areas where there are very few WC reinforcements, where the tribolayer has difficulties to form. Therefore, wear phenomenon will be accelerated in local areas of the track, where high depth and width will be reached (Fig. 2b). Moreover, since the WC reinforcements protect only the areas behind them with respect to sliding direction, big holes ahead of the WC reinforcements will appear on the surface (Fig. 5g). Consequently, the severe wear will lead to a final high wear rate (Fig. 2a). Another phenomenon involving ball inertia, the lack of protective tribolayer in areas with low surface density of WC reinforcements, and the drop in CoF in combination with a ball jump, may also explain the higher worn volume observed when using the WC-6Co ball compared to Si_3N_4 ball (*Fig. 2*b). This phenomenon has been studied by [64], with similar sequences, but mainly present on the ball side rather than the substrate side.

4.1.3 Tribo-chemical wear with Si_3N_4

The regular and smooth track formed with Si_3N_4 as counter-body after the reference test is the result of a mild wear (Fig. 4g) which is influenced by the chemical nature of the tribolayer that is formed. Indeed, as it will be better explained in section 4.2, there is a chemical affinity between Si_3N_4 and the MMC specimen. When considering Si_3N_4 as counter-body, it appears that within such tribosystem the WC reinforcements do not influence the formation of the tribolayer (Fig. 4), contrarily to what happened with WC-6Co. Indeed, the collapse of the CoF ('1st Drop' in Fig. 3a) is associated with the adhesion of Si-rich debris from the counter-body to the surface of the specimen, which become Si-rich oxides (Fig. 4c-d). It can be assumed that SiO_2 is formed, as the result of the oxidation of Si that has been released [65,66]. SiO_2 is known as an amorphous phase, which may explain why it is hard to detect it based on the XRD analysis carried out on debris (Fig. 10). Once present, Si-rich oxides will create a protective layer between counter-body and MMC, thus decreasing friction and wear. Moreover, as explained subsequently in section 4.2, the presence of Si helps the stabilization of the Cr_2O_3 layer of the specimen. Therefore, the wear mechanism involved using Si_3N_4 as counter-body is a tribo-chemical reaction between counter-body and MMC. Following the first drop of CoF due to the presence of a stable tribolayer, the Si-rich oxides will start mixing with Cr_2O_3 leading to a compact layer. After few sharp drops and rises ('3rd Rise' in Fig. 3a), the CoF will stabilize at a high value. Indeed, even if Cr_2O_3 can achieve good wear protection, its ability to reduce the CoF is limited [67]. When the compaction reaches a limit, the tribolayer is torn and many sharp debris is generated (Fig. 4e-f and Fig. 9a), affecting the CoF and

PDe with many fluctuations (end of 'Stabilization' period in Fig. 3a). The direct contact between counter-body and specimen allows the adhesion of new Si-rich material from the counter-body to the surface of the specimen, with the restoration of the protective properties of tribolayer that will decrease the friction (indicated as '2nd Drop' in Fig. 3a). Subsequently, the mixing and compaction of the new Si-rich oxides with Cr_2O_3 lead to the increase of the CoF (indicated as '4th Rise' in Fig. 3a) up to a stabilization at high values. With Si_3N_4, the period during which the tribolayer plays a protective role against the MMC specimen is longer compared to the one occurring with WC-6Co. The time duration of the protective stage is indeed related to the occurrence of the stabilized tribolayer, which starts straight after the run-in period and ends with the cyclical regime. Else, there is direct contact between specimen and counter-body that enhance the wear rate. This observation is also validated by the reduced length of the run-in period with Si_3N_4, which is almost four times shorter than with WC-6Co as counter-body.

Therefore, with Si_3N_4, Cr and Si rich oxides allow a continuous protection of the subsurface. Thus, a thick and homogeneous MML can form in a large portion of the subsurface (Fig. 6a-c). Moreover, since oxides are always present, they penetrate in the subsurface enriching the MML and enhancing the wear protection (Fig. 6c-e). In contrast, with WC-6Co as counter-body, oxides penetrate only in the holes left ahead of cracked and pulled out WC reinforcements (Fig. 6f). The high protective properties of the tribolayer and MML formed with Si_3N_4 allow for the PDL to not be exposed and thus, the formation of corrosive compounds is avoided. Indeed, only few orange pieces of debris were visible after the reference test and mostly green debris were collected, that is the typical colour of Cr_2O_3 (Fig. 9b).

Fig. 11 summarizes the wear phenomena observed when using WC-6Co and Si_3N_4 and as counter-body with MMC specimen beneath, that lead to a tribo-corrosive and to a tribo-chemical wear mechanism respectively. Such a sketch of wear mechanisms illustrates not only the continuous or discontinuous nature of the tribolayer, but also the extent of both MML and PDL below the wear track.

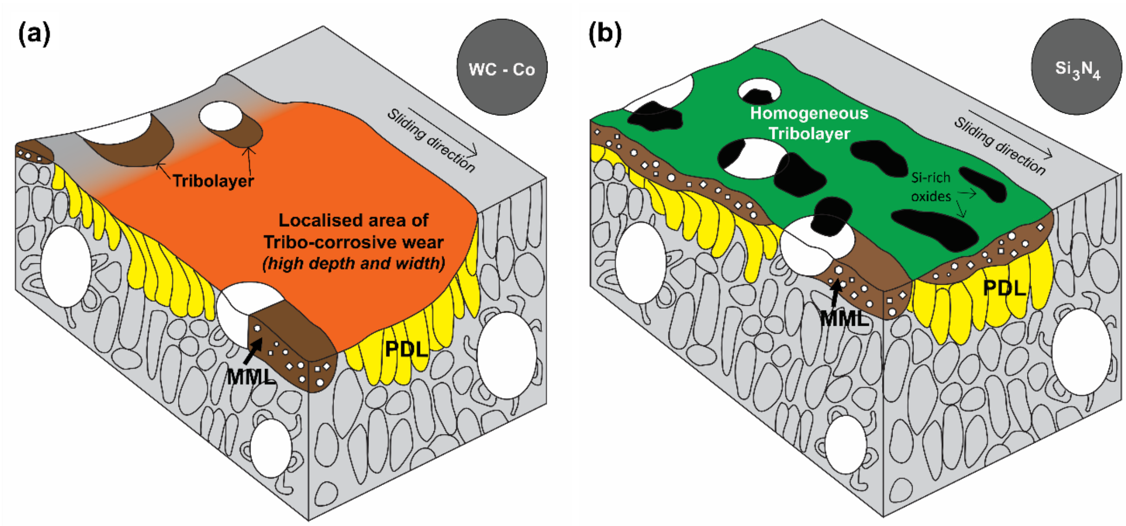

Fig. 11 : Tribo-corrosive wear mechanism using WC-6Co (a) and Tribo-chemical wear mechanism using Si_3N_4 (b).

4.2 Influence of the counter-body on the wear behavior on the tribolayer formation and run-in length

For a more extended and comprehensive investigation, results using Al_2O_3 and 440C as additional counter-bodies are included in this section.

4.2.1 Wear rates influenced by counter-body nature

The wear rates obtained on both counter-bodies and substrate are shown for comparison in Fig. A.1 within the supplementary material (Appendix A). Wear tests based on Al_2O_3 have been explained within a previous work [16]. A reminder of the cyclical regime features is given in Fig. A.2 and an illustration of the wear sequence and related mechanisms arisen with Al_2O_3 counter-body are shown in Fig. A.3. For the wear campaign using 440C counter-body, details can also be found within the supplementary material (Appendix A). There is an increasing trend in counter-body wear when changing from WC-6Co to Si_3N_4, 440C and finally Al_2O_3 respectively, with the least worn counter-body (WC-6Co) having a wear rate almost 10 times lower than the next most worn counter-body made of Si_3N_4.

Meanwhile, wear rates on DEDed 316L+WC MMC show two trends for all four tribosystems, namely a relatively low wear rate when tested either against Si_3N_4 or 440C, and a wear rate twice as high if tested either against WC-6Co or Al_2O_3.

A tribo-corrosive wear mechanism similar to the one previously highlighted with WC-6Co counter-body (section 4.1.2) also occurs while using Al_2O_3 as counter-body. Indeed, during the test with Al_2O_3 a tribolayer characterized by many U-shape islands is formed and broken down cyclically leading to a high wear rate of the specimen under a tribo-corrosive wear mechanism. Full explanation of the wear sequence can be found in our previous work [16]. Instead, using 440C as counter-body, low wear rates of the specimen were measured (Fig. A.1 in Appendix A) due to the occurrence of wear phenomena similar to that of the test with Si_3N_4 as counter-body, even if no cyclical segments within the CoF trend were observed (Fig. A.4 in Appendix A). Indeed, with 440C counter-body, the protective tribolayer which looks homogeneous and stable after the run-in period (Fig. A.4 in Appendix A) remains as such over the duration of the reference test (Fig. A.3 in Appendix A). Therefore, the tribolayer protects the MMC throughout the wear test, enabling the formation of a thick and homogeneous MML above a slightly thicker PDL (Fig. A.6 in Appendix A) that are similar to the ones obtained with Si_3N_4 as counter-body.

4.2.2 Counter-bodies influencing wear track morphology and wear debris

With WC-6Co, the tribo-corrosive wear mechanism will accelerate the wear of the specimen, where a high track depth is achieved. These areas correspond to regions of the track with few WC reinforcements, where little to no tribolayer is present that can protect the surface from wear.

Conversely, with Si_3N_4 counter-body, the tribolayer is homogeneously present over the worn track, thus promoting a homogeneous track width (*Fig. 2*)

At the macro-scale, changing the counter-body mainly caused a different width of the track. With WC-6Co, a higher depth was achieved compared to that obtained with Si_3N_4, in view of local tribo-corrosive wear mechanism that accelerated the wear in areas with few WC reinforcements. The characterization of debris at the macro-scale revealed that compacted debris with sharp edges is found only for the test ran while using Si_3N_4, whereas a U-shape island of compacted oxides is present when considering WC-6Co as counter-body. The two different types of debris are formed according to the type of tribolayer formed.

Further decreasing the scale of observation at the nanoscale, the nanoscopic Cr_2O_3 layer present on the surface of the DEDed 316L+WC composite promoted the protection thanks to its ability of Si adsorption coming from the counter-body. XRD analysis on debris revealed the presence of Cr_2O_3.

4.2.3 Counter-body properties influencing wear regimes

Even if the overall wear mechanism of each tribosystem is affected by many friction-induced phenomena that occur at different scales, the run-in period is found to be mainly influenced by the mechanical and chemical properties of the counter-body that is used. Indeed, combining the mechanical properties (Table 1) and the measurements on the worn volume of the counter-bodies (Fig. 2a), there is a clear relation between both plasticity and brittleness index on one hand, and wear of the counter-body on the other hand (Fig. 12a). In particular, the lower indexes of WC-6Co lead to a lower wear rate of this counter-body compared to the others. Therefore, very few debris are generated from WC-6Co. On the contrary, with Al_2O_3, Si_3N_4 and 440C, the total wear rate of the counter-body is high and thus, debris from the counter-body are expected to be spread along the surface of the specimen, participating in the formation of the tribolayer as explained in section 4.1.1. Therefore, the stabilization of the tribolayer is faster using Al_2O_3, Si_3N_4 and 440C compared to WC-6Co. As a general rule, decreasing both the toughness and the stiffness of the counter-body will lead to an increase of the wear rate with the more debris that is generated. At the same time, the formation and stabilization of the tribolayer will be speeded thus yielding a decrease of the length of the run-in period (Fig. 12b).

4.2.4 Qualitative approaches for quick identification of wear regimes based on counter-body properties and wear debris nature

At this stage, it can be stated that two new approaches which are complementary to CoF analysis can be considered if different regimes must be distinguished during wear tests.

The first approach may consider both plasticity and brittleness indexes of the counter-body to set a straight correlation with the wear behaviour of composite materials. This link is established in terms of the duration of the run-in period, which is itself linked to the higher wear rate of the counter-body occurring during this phase. Then, the formation of a tribolayer begins, whose stability lowers the wear rate under a steady-state regime.

The second approach is based on the nature of the debris formed during the wear test, their colour being considered as a quick distinction criterion. Debris always looks dark at the end of the run-in period, regardless of the counter-body that is been considered. Subsequently, the colour of the debris will change depending on both the counter-body and the wear mechanism involved. Debris is orange and black when using both Al_2O_3 and WC-6Co as counter-bodies. Else, with Si_3N_4 and 440C as counter-bodies, debris is green/orange (Fig. 9) and brownish red respectively (Fig. A.5 in Appendix A).

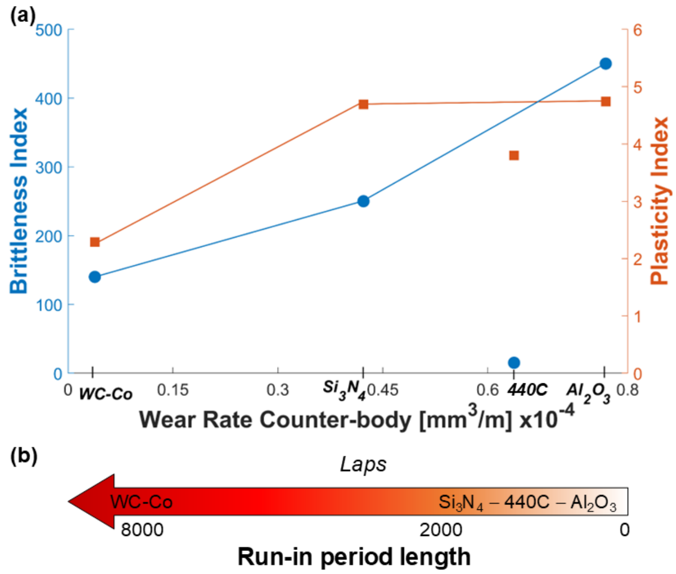

Fig. 12 : Influence of the mechanical properties of different counter-bodies on the Wear Rate (a) and on the length of the Run-in period (b)

In addition, as for the test with Si_3N_4 as counter-body, a tribo-chemical wear mechanism can shorten the run-in period. This tribo-chemical reaction is probably due to the interaction between the protective surface layer that forms naturally on stainless steels, and the Si-rich particles previously broken away from the counter-body during the wear test. Indeed, it has been established that Si, Mo or rare earth elements improve the adhesion of Cr_2O_3 [66,67]. Therefore, the use of Si_3N_4 will promote the occurrence of Si-rich debris (Fig. 4a-b), which will react with the Cr_2O_3 also present on the surface of the DEDed 316L+WC MMC. It is because such a tribo-chemical reaction occurs very early during the wear test that a stable tribolayer will also be formed very quickly. Consequently, the run-in period will be significantly shortened.

4.3 Enhancing the hierarchical structure feature role upon wear mechanisms

In addition to defining hierarchical structures, Zhai et al. [5]have shown in their work that different wear mechanisms acting simultaneously over various scales and hierarchy levels result in the hierarchical and heterogeneous nature of wear. Therefore, the design of heterogeneous hierarchical structures makes it possible to achieve tribological properties within the surface and/or in the core of the materials under consideration, which can help improving the wear based on the scale of interaction.

In the case of DEDed 316L+WC MMC, several scale levels set its hierarchical structure. First, there are undissolved WC reinforcements that represent the reference structure on a macroscopic scale. Then, at the mesoscopic scale, solidification carbides can be found, which are made of elements coming from the dissolution of WC reinforcements when they are heated up by the laser beam, or when they are inside the melt pool. And finally at the micro-scale, there is the matrix that undergoes solid solution strengthening from elements coming from both the WC reinforcements and the melted stainless-steel powder.

*4.3.1 **Undissolved WC reinforcements role at the macro-scale***

The undissolved WC reinforcements that are also known as ex-situ carbides because of their inheritance from the initial powder [6], will play a role at the macro-scale. Firstly, they will promote tribolayer formation by accumulating debris in the form of U-shaped islands, especially when the counter-bodies are WC-6Co or Al_2O_3. In such cases, a tribo-corrosive wear mechanism will occur at the macro-scale. Conversely, the WC reinforcements will not influence the tribolayer formation if either Si_3N_4 or 440C are considered as counter-bodies, as a tribo-chemical reaction will occur straight between the matrix and the counter-body. In this case, within the tribolayer, MML will be enriched with fractured solidification carbides that will protect the friction-induced martensite present within PDL beneath. In addition, with Si_3N_4 as counter-body, the nanoscopic Cr_2O_3 layer present on the surface of the DEDed 316L+WC composite will exhibit an enhanced protection thanks to the adsorption of Si coming from the counter-body [66,67].

Moreover, the undissolved WC reinforcements will strongly influence the counter-body wear unless the latter is made of the same material (WC-6Co counter-body).

4.3.2 *Solidification carbides role at the meso-scale*

The solidification carbides that are also known as in-situ carbides that originated from a chemical reaction during the fabrication [6] will play a role at the meso-scale. The carbides, which are also ascribed to cell boundaries within the hierarchical structure will improve the local matrix strength through dislocation pile-up and local hardening, both phenomena being more likely to occur in PDL regions, regardless of the counter-body [5,34].

4.3.3 *Matrix role at both micro- and nanoscale*

At both micro- and nano-scale, solid solution strengthening is achieved within the matrix, due to its supersaturation that can lead to significant distortions within crystal lattices [16]. The subsequent severe plastic deformation of the matrix that occurs in both MML and PDL regions will trigger austenite to martensite transformation regardless of the counter-body [21] leading to transformation induced plasticity or TRIP-like phenomenon.

4.4 Tribosystem as all to allow wear mechanisms enhancement

Wear mechanisms cannot be identified only considering the properties of the counter-bodies alone. It is indeed necessary to consider the overall tribosystem, including complex phenomena occurring between counter-body and specimen. That obviously applies even more when the specimen is made of an MMC. In fact, a given counter-body can lead to different wear mechanisms if tested with different specimen materials. Therefore, it is important to consider the response of the specimen to the solicitation of a defined counter-body.

In this case, the specific properties of WC-6Co and Si_3N_4 that mainly contribute to the identification of the wear mechanisms when used against DEDed MMC are mechanical properties and chemical properties respectively. The first are responsible for the high wear of the specimen, which causes the generation of many debris. The latter remains blocked by the WC reinforcements of the specimen, participating in the formation of the tribolayer. Therefore, for the tribosystem WC-6Co/DED 316L+WC, the tribo-corrosive mechanism is the combination of mechanical properties of WC-6Co counter-body and the presence of WC reinforcements on the specimen. In contrast, for the tribosystem Si_3N_4/DED 316L+WC, the tribochemical wear mechanism is the result of a tribochemical reaction between elements from the counter-body (Si) and from the specimen (Cr).

Ultimately, this study shows that understanding the highly complex tribological behaviour of a DEDed MMC based on a simplified distinction among the existing wear phenomena is possible. For this purpose, tribosystems pertaining to both the scale of analysis and the corresponding feature within the hierarchical structure of the MMC should be defined to help highlighting the related wear mechanisms. Such an approach can be a powerful tool for designing hierarchical microstructures with enhanced wear properties via additive manufacturing processes.

4.5 Possible applications for the future

Within this work, the feasibility of an Additive manufacturing production method for a MMC deposit under a 316L stainless steel substrate has been demonstrated. Such a deposit exhibits enhanced tribological properties. Nevertheless, the substrate used in the present work should not be considered as a limiting factor. In fact, any other material apart from 316L stainless steel that can have a defect-free metallurgical bond together with a good physico-chemical compatibility (thermal conductivity and chemical affinity) with the deposit can be a good candidate.

DED processes have been so far involved within refurbishing and repairing of cutting tools or drill bits, especially when processing with the deposition of a MMC coating on a substrate to yield improved wear and toughness properties [68–70]. Furthermore, Functionally Graded Materials (FGM) can also be developed using DED process for production of MMC, thanks to the ability of controlling the composition and optimizing the properties of the built part, especially for applications in the military or the aerospace fields where extremely high temperatures are to be sustained [71,72].

5. Conclusions

- DEDed MMC 316L+WC tested with different counter-bodies corresponds to different complex tribosystems. Dry sliding tests on these tribosystems give distinct wear rates on both the specimen and the counter-body.
- Complex tribosystems based on DEDed MMC can lead to cyclic wear regimes. In such cases, tribolayer formation, stabilization and cracking are the most relevant physical criteria for distinguishing the run-in and steady-state phases within the wear regime. The nature of the debris can also be a secondary means of distinguishing the cyclic phases of the wear regime.
- The duration of the run-in phase increases with decreasing values of the counter-body brittleness and plasticity indices. However, there is an inverse correlation between the values of these indices and the wear rate of the counter-body.
- Two wear mechanisms can be determined within complex tribosystems including DEDed MMC. A mild tribo-chemical wear mechanism when considering the Si_3N_4 and the 440C counterparts, and a severe tribo-corrosive wear mechanism when considering the WC-6Co and the Al_2O_3 counter-bodies.
- The metallurgical changes in the DEDed MMC sublayers beneath the wear track are also related to the wear mechanisms. In this case, the MML and PDL will have a greater extent and better resistance with tribo-chemical wear than with tribo-corrosive wear.

- The hierarchical structures of DEDed MMC 316L+WC play an important role in the wear mechanisms. At the macroscopic level, undissolved WC reinforcements will lead to the tribo-corrosive mechanism observed with both WC-6Co or Al_2O_3 counter-bodies. At the meso-scale, solidification carbides will improve the matrix strength regarless of the counter-body used. At the micro- or nano-scale, matrix will promote solution strengthening prior to TRIP-like phenomenon, whereas as its interaction with surface oxide will yield a tribo-chemical mechanism that is observed with Si_3N_4 and 440C counter-bodies.

Acknowledgements

This work was supported by the FNRS (Fonds National de la Recherche Scientifique of Belgium, PDR number 35298295) and by the European Fund for Regional Development and the Walloon Region under convention FEDER "Iawatha". The authors acknowledge the CAREM of the Uliège for providing SEM/EDS/EBSD facilities. They also thank Sylvie Salieri for the samples preparation, Samuel Rondia for the substrates preparation and the Sirris Research Center for access to DED equipment.

References

[1] So H. Characteristics of wear results tested by pin-on-disc at moderate to high speeds. Tribology International 1996;29:415–23. https://doi.org/10.1016/0301-679X(95)00097-N.

[2] Ashby MF, Lim SC. Wear-mechanism maps. Scripta Metallurgica et Materialia 1990;24:805–10. https://doi.org/10.1016/0956-716X(90)90116-X.

[3] Wilson S, Alpas AT. Wear mechanism maps for metal matrix composites. Wear 1997;212:41–9. https://doi.org/10.1016/S0043-1648(97)00142-7.

[4] Blau PJ. Fifty years of research on the wear of metals. Tribology International 1997;30:321–31. https://doi.org/10.1016/S0301-679X(96)00062-X.

[5] Zhai W, Bai L, Zhou R, Fan X, Kang G, Liu Y, et al. Recent Progress on Wear-Resistant Materials: Designs, Properties, and Applications. Advanced Science 2021;8:2003739. https://doi.org/10.1002/advs.202003739.

[6] Mertens AI, Lecomte-Beckers J, Mertens AI, Lecomte-Beckers J. On the Role of Interfacial Reactions, Dissolution and Secondary Precipitation During the Laser Additive Manufacturing of Metal Matrix Composites: A Review. New Trends in 3D Printing, IntechOpen; 2016. https://doi.org/10.5772/63045.

[7] Liao Z, Huang X, Zhang F, Li Z, Chen S, Shan Q. Effect of WC mass fraction on the microstructure and frictional wear properties of WC/Fe matrix composites. International Journal of Refractory Metals and Hard Materials 2023;114:106265. https://doi.org/10.1016/j.ijrmhm.2023.106265.
[8] Pal J, Gupta D, Singh TP. Influence of WC-12Co reinforcement on sliding wear performance of stainless steel-based MMC processed in a microwave oven. Proceedings of the Institution of Mechanical Engineers, Part C 2024;238:6643–72. https://doi.org/10.1177/09544062241228389.
[9] Behera MP, Dougherty T, Singamneni S. Conventional and Additive Manufacturing with Metal Matrix Composites: A Perspective. Procedia Manufacturing 2019;30:159–66. https://doi.org/10.1016/j.promfg.2019.02.023.
[10] Lu JZ, Cao J, Lu HF, Zhang LY, Luo KY. Wear properties and microstructural analyses of Fe-based coatings with various WC contents on H13 die steel by laser cladding. Surface and Coatings Technology 2019;369:228–37. https://doi.org/10.1016/j.surfcoat.2019.04.063.
[11] Li H, Hu Y, Di R, Yuan R, Shi C, Lei J. Effects of WC particles on microstructure and mechanical properties of 316L steel obtained by laser melting deposition. Ceramics International 2022;48:20388–99. https://doi.org/10.1016/j.ceramint.2022.03.324.
[12] Cao Q, Fan L, Chen H, Hou Y, Dong L, Ni Z. Wear behavior of laser cladded WC-reinforced Ni-based coatings under low temperature. Tribology International 2022;176:107939. https://doi.org/10.1016/j.triboint.2022.107939.
[13] Deenadayalan K, Murali V, Elayaperumal A, Satheesh kumar A, Arulvel S, Shahedi Asl M. Friction and wear properties of short time heat-treated and laser surface re-melted NiCr-WC composite coatings at various dry sliding conditions. Journal of Materials Research and Technology 2022;17:3080–104. https://doi.org/10.1016/j.jmrt.2022.01.124.
[14] Ostolaza M, Arrizubieta JI, Lamikiz A, Ukar E. Study of the flexural behaviour and bonding strength of WC-Co metal matrix composite coatings produced by Laser Directed Energy Deposition. Surface and Coatings Technology 2023;463:129538. https://doi.org/10.1016/j.surfcoat.2023.129538.
[15] Wang H, Liu K, Li J, Geng S, Jing L, Skuratov V. Reinforcements/matrix micro-interface evolution and properties of in-situ Ni60A/WC coatings prepared by laser cladding. Surface and Coatings Technology 2024;484:130834. https://doi.org/10.1016/j.surfcoat.2024.130834.
[16] Maurizi Enrici T, Dedry O, Boschini F, Tchuindjang JT, Mertens A. Microstructural and Thermal Characterization of 316L + WC Composite Coatings Obtained by Laser Cladding. Advanced Engineering Materials 2020;22:2000291. https://doi.org/10.1002/adem.202000291.
[17] Fetni S, Enrici TM, Niccolini T, Tran HS, Dedry O, Duchêne L, et al. Thermal model for the directed energy deposition of composite coatings of 316L stainless steel enriched with tungsten carbides. Materials & Design 2021;204:109661. https://doi.org/10.1016/j.matdes.2021.109661.
[18] Maurizi Enrici T, Mario D, Dedry O, Castagne S, Mertens A, Tchuindjang JT. Unveiling the complex wear sequence of a directed energy deposited 316L+WC hierarchical composite against alumina. Journal of Materials Research and Technology 2023;26:621–38. https://doi.org/10.1016/j.jmrt.2023.07.172.
[19] Hashemi N, Mertens A, Montrieux H-M, Tchuindjang JT, Dedry O, Carrus R, et al. Oxidative wear behaviour of laser clad High Speed Steel thick deposits: Influence of sliding speed, carbide type and morphology. Surface and Coatings Technology 2017;315:519–29. https://doi.org/10.1016/j.surfcoat.2017.02.071.
[20] Miyajima T, Sasayama S, Honda T, Fuwa Y, Iwai Y. Effects of Hardness of Counterface on Dry Sliding Wear of Aluminum Matrix Composites against Steels. Tribology Online 2012;7:24–32. https://doi.org/10.2474/trol.7.24.
[21] Perret J, Boehm-Courjault E, Cantoni M, Mischler S, Beaudouin A, Chitty W, et al. EBSD, SEM and FIB characterisation of subsurface deformation during tribocorrosion of stainless steel in sulphuric acid. Wear 2010;269:383–93. https://doi.org/10.1016/j.wear.2010.04.023.

[22] Küçük Y. Effect of counterbody on the dry sliding wear performance of plasma sprayed calcia-stabilized zirconia coating. International Journal of Refractory Metals and Hard Materials 2020;92:105284. https://doi.org/10.1016/j.ijrmhm.2020.105284.
[23] Zhang W, Yamashita S, Kita H. Effect of counterbody on tribological properties of B4C–SiC composite ceramics. Wear 2020;458–459:203418. https://doi.org/10.1016/j.wear.2020.203418.
[24] Zeng Z, Wang L, Chen L, Zhang J. The correlation between the hardness and tribological behaviour of electroplated chromium coatings sliding against ceramic and steel counterparts. Surface and Coatings Technology 2006;201:2282–8. https://doi.org/10.1016/j.surfcoat.2006.03.038.
[25] Leyland A, Matthews A. On the significance of the *H*/*E* ratio in wear control: a nanocomposite coating approach to optimised tribological behaviour. Wear 2000;246:1–11. https://doi.org/10.1016/S0043-1648(00)00488-9.
[26] Kovalčíková A, Kurek P, Balko J, Dusza J, Šajgalík P, Mihaliková M. Effect of the counterpart material on wear characteristics of silicon carbide ceramics. International Journal of Refractory Metals and Hard Materials 2014;44:12–8. https://doi.org/10.1016/j.ijrmhm.2014.01.006.
[27] Guicciardi S, Sciti D, Melandri C, Pezzotti G. Dry sliding wear behavior of nano-sized SiC pins against SiC and Si3N4 discs. Wear 2007;262:529–35. https://doi.org/10.1016/j.wear.2006.06.009.
[28] Bhosale DG, Rathod WS, Rukhande SW. Effect of counter faces on sliding wear behavior of WC-Cr3C2-Ni composite coating deposited by high velocity oxy fuel. Materials Today: Proceedings 2021;41:780–5. https://doi.org/10.1016/j.matpr.2020.08.466.
[29] Blau PJ. On the nature of running-in. Tribology International 2005;38:1007–12. https://doi.org/10.1016/j.triboint.2005.07.020.
[30] Chen G, Wei Y, Li S, Zhou W. Friction and wear mechanism of unlubricated 304L austenitic stainless steel at room temperature. J Wuhan Univ Technol-Mat Sci Edit 2012;27:222–6. https://doi.org/10.1007/s11595-012-0441-3.
[31] Quinn TFJ. Review of oxidational wear: Part I: The origins of oxidational wear. Tribology International 1983;16:257–71. https://doi.org/10.1016/0301-679X(83)90086-5.
[32] Wilson JE, Stott FH, Wood GC, Tabor D. The development of wear-protective oxides and their influence on sliding friction. Proceedings of the Royal Society of London A Mathematical and Physical Sciences 1997;369:557–74. https://doi.org/10.1098/rspa.1980.0016.
[33] Bahshwan M, Myant CW, Reddyhoff T, Pham M-S. The role of microstructure on wear mechanisms and anisotropy of additively manufactured 316L stainless steel in dry sliding. Materials & Design 2020;196:109076. https://doi.org/10.1016/j.matdes.2020.109076.
[34] Wu X, Meng F, Baker I, Wu H, Munroe PR. An Overview of Dry Sliding Wear of Two-Phase FeNiMnAl Alloys. MRS Online Proceedings Library 2013;1516:103–8. https://doi.org/10.1557/opl.2012.1681.
[35] Lee Y-S, Kondo Y, Okayasu M. Friction-Induced Martensitic Transformation and Wear Properties of Stainless Steel under Dry and Wet Conditions. Metals 2020;10:743. https://doi.org/10.3390/met10060743.
[36] Prasad CD, Jerri A, Ramesh MR. Characterization and Sliding Wear Behavior of Iron-Based Metallic Coating Deposited by HVOF Process on Low-Carbon Steel Substrate. J Bio Tribo Corros 2020;6:69. https://doi.org/10.1007/s40735-020-00366-7.
[37] So H. The mechanism of oxidational wear. Wear 1995;184:161–7. https://doi.org/10.1016/0043-1648(94)06569-1.
[38] Rigney DA. Comments on the sliding wear of metals. Tribology International 1997;30:361–7. https://doi.org/10.1016/S0301-679X(96)00065-5.
[39] Garza-Montes-de-Oca NF, Rainforth WM. Wear mechanisms experienced by a work roll grade high speed steel under different environmental conditions. Wear 2009;267:441–8. https://doi.org/10.1016/j.wear.2009.01.048.

[40] Yin C, Liang Y, Liang Y, Li W, Yang M. Formation of a self-lubricating layer by oxidation and solid-state amorphization of nano-lamellar microstructures during dry sliding wear tests. Acta Materialia 2019;166:208–20. https://doi.org/10.1016/j.actamat.2018.12.049.
[41] Yin C, Liang Y, Jiang Y, Yang M, Long S. Formation of nano-laminated structures in a dry sliding wear-induced layer under different wear mechanisms of 20CrNi2Mo steel. Applied Surface Science 2017;423:305–13. https://doi.org/10.1016/j.apsusc.2017.06.187.
[42] Casellas D, Caro J, Molas S, Prado JM, Valls I. Fracture toughness of carbides in tool steels evaluated by nanoindentation. Acta Materialia 2007;55:4277–86. https://doi.org/10.1016/j.actamat.2007.03.028.
[43] J AR, Kailas SV. Evolution of wear debris morphology during dry sliding of Ti–6Al–4V against SS316L under ambient and vacuum conditions. Wear 2020;456–457:203378. https://doi.org/10.1016/j.wear.2020.203378.
[44] Smith AF. The friction and sliding wear of unlubricated 316 stainless steel in air at room temperature in the load range 0.5–90 N. Wear 1986;110:151–68. https://doi.org/10.1016/0043-1648(86)90143-2.
[45] Brin C, Rivière J-P, Eymery J-P, Villain J-P. Structural Characterization of Wear Debris Produced During Friction Between Two Austenitic Stainless Steel Antagonists. Tribology Letters 2001;11:127–32. https://doi.org/10.1023/A:1016612718139.
[46] Li CX, Xia J, Dong H. Sliding wear of TiAl intermetallics against steel and ceramics of Al2O3, Si3N4 and WC/Co. Wear 2006;261:693–701. https://doi.org/10.1016/j.wear.2006.01.044.
[47] Xingzhong Z, Jiajun L, Baoliang Z, Hezhou M, Zhenbi L. Wear behavior of Si3N4 ceramic cutting tool material against stainless steel in dry and water-lubricated conditions. Ceramics International 1999;25:309–15. https://doi.org/10.1016/S0272-8842(98)00040-6.
[48] Li XY, Tandon KN. Amorphization and precipitation within the amorphous layer induced by dry sliding wear of an A-Si/SiCp composite material. Acta Materialia 1996;44:3611–24. https://doi.org/10.1016/1359-6454(96)00001-8.
[49] Jiang J, Stott FH, Stack MM. The role of triboparticulates in dry sliding wear. Tribology International 1998;31:245–56. https://doi.org/10.1016/S0301-679X(98)00027-9.
[50] Stott FH, Wood GC. The influence of oxides on the friction and wear of alloys. Tribology International 1978;11:211–8. https://doi.org/10.1016/0301-679X(78)90178-0.
[51] Rabinowicz E. Lubrication of Metal Surfaces by Oxide Films. A S L E Transactions 1967;10:400–7. https://doi.org/10.1080/05698196708972199.
[52] Suh NP. An overview of the delamination theory of wear. Wear 1977;44:1–16. https://doi.org/10.1016/0043-1648(77)90081-3.
[53] Kalin M. Influence of flash temperatures on the tribological behaviour in low-speed sliding: a review. Materials Science and Engineering: A 2004;374:390–7. https://doi.org/10.1016/j.msea.2004.03.031.
[54] Kato H. Severe–mild wear transition by supply of oxide particles on sliding surface. Wear 2003;255:426–9. https://doi.org/10.1016/S0043-1648(03)00077-2.
[55] Rainforth WM, Leonard AJ, Perrin C, Bedolla-Jacuinde A, Wang Y, Jones H, et al. High resolution observations of friction-induced oxide and its interaction with the worn surface. Tribology International 2002;35:731–48. https://doi.org/10.1016/S0301-679X(02)00040-3.
[56] McEvily AJ, Gonzalez Velazquez JL. Fatigue crack tip deformation Processes as Influenced by the Environment. Metall Trans A 1992;23:2211–21. https://doi.org/10.1007/BF02646014.
[57] Breedis JF, Kaufman L. Formation of Hcp and Bcc phases in austenitic iron alloys. Metall Trans 1971;2:3249–3249. https://doi.org/10.1007/BF02814993.
[58] Hsu K-L, Ahn TM, Rigney DA. Friction, wear and microstructure of unlubricated austenitic stainless steels. Wear 1980;60:13–37. https://doi.org/10.1016/0043-1648(80)90247-1.

[59] Hirth JP, Rigney DA. Crystal plasticity and the delamination theory of wear. Wear 1976;39:133–41. https://doi.org/10.1016/0043-1648(76)90229-5.
[60] Ishida K. Effect of magnetic transformation on stacking fault energy of nickel binary alloys. The Philosophical Magazine: A Journal of Theoretical Experimental and Applied Physics 1975;32:663–9. https://doi.org/10.1080/14786437508220887.
[61] Talha M, Ma Y, Lin Y, Pan Y, Kong X, Sinha OP, et al. Corrosion performance of cold deformed austenitic stainless steels for biomedical applications. Corrosion Reviews 2019;37:283–306. https://doi.org/10.1515/corrrev-2019-0004.
[62] Pedrosa J, Costa BFO, Portugal A, Durães L. Controlled phase formation of nanocrystalline iron oxides/hydroxides in solution – An insight on the phase transformation mechanisms. Materials Chemistry and Physics 2015;163:88–98. https://doi.org/10.1016/j.matchemphys.2015.07.018.
[63] Ravikiran A, Bai BNP. Influence of Speed on the Tribochemical Reaction Products and the Associated Transitions for the Dry Sliding of Silicon Nitride against Steel. Journal of the American Ceramic Society 1995;78:3025–32. https://doi.org/10.1111/j.1151-2916.1995.tb09078.x.
[64] Antonov M, Hussainova I, Adoberg E. Effect of loading system inertia on tribological behaviour of ceramic–ceramic, ceramic–metal and metal–metal dry sliding contacts. Tribology International 2013;65:207–14. https://doi.org/10.1016/j.triboint.2013.03.025.
[65] Fischer TE, Tomizawa H. Interaction of tribochemistry and microfracture in the friction and wear of silicon nitride. Wear 1985;105:29–45. https://doi.org/10.1016/0043-1648(85)90004-3.
[66] Cheng X, Jiang Z, Wei D, Wu H, Jiang L. Adhesion, friction and wear analysis of a chromium oxide scale on a ferritic stainless steel. Wear 2019;426–427:1212–21. https://doi.org/10.1016/j.wear.2019.01.045.
[67] Sand T, Edgren A, Geers C, Asokan V, Eklund J, Helander T, et al. Exploring the Effect of Silicon on the High Temperature Corrosion of Lean FeCrAl Alloys in Humid Air. Oxid Met 2021;95:221–38. https://doi.org/10.1007/s11085-020-10019-2.
[68] Piri M, Hashemolhosseini H, Mikaeil R, Ataei M, Baghbanan A. Investigation of wear resistance of drill bits with WC, Diamond-DLC, and TiAlSi coatings with respect to mechanical properties of rock. International Journal of Refractory Metals and Hard Materials 2020;87:105113. https://doi.org/10.1016/j.ijrmhm.2019.105113.
[69] Zhang Y, Sogn H, Cai M, Santana R. An Additive Manufacturing Process Enables the 3D-Printed Application of Armors for Drill Bits, OnePetro; 2023. https://doi.org/10.2118/214548-MS.
[70] Bhat C, Jiang ,Cho-Pei, Shan Romario ,Yulius, Paral ,Sandeep Kumar, and Toyserkani E. Critical review of metal-ceramic composites fabricated through additive manufacturing for extreme condition applications. Mechanics of Advanced Materials and Structures 2025;32:2153–80. https://doi.org/10.1080/15376494.2024.2376337.
[71] Hegab HA. Design for additive manufacturing of composite materials and potential alloys: a review. Manufacturing Rev 2016;3:11. https://doi.org/10.1051/mfreview/2016010.
[72] Gualtieri T, Bandyopadhyay A. Additive manufacturing of compositionally gradient metal-ceramic structures: Stainless steel to vanadium carbide. Materials & Design 2018;139:419–28. https://doi.org/10.1016/j.matdes.2017.11.007.